WILEY | Hindawi

Research Article
Mechanism of Forming Low Resistivity in Shale Reservoirs

Jirong Xie,[1,2] Jiahuan He [ID],[2,3,4] Keming Zhou,[2,3] Zhijuan Tang,[3] Manfei Chen,[2,3] Tingting He,[3] Mengwen Zou,[3] Tao Luo,[3] Nong Li,[2,3,4] and Li Wang[3]

[1]*PetroChina Southwest Oil and Gas Field Company, Chengdu, China*
[2]*Shale Gas Evaluation and Exploitation Key Laboratory of Sichuan Province, Chengdu, China*
[3]*Institute of Exploration and Development, PetroChina Southwest Oil and Gas Field Company, Chengdu, China*
[4]*Sichuan Kelite Oil and Gas Technology Service Limited Company, Chengdu, China*

Correspondence should be addressed to Jiahuan He; 406768590@qq.com

In the oil and gas industry, traditional logging mostly deems that oil and gas reservoirs are characterized by high resistivity, whereas the water layer is often by low resistivity. However, a lot of exploration and development practices on shale gas reservoirs in Sichuan Basin, China, prove that it is hard to characterize a functional relation between resistivity and water saturation using the Archie equation. Therefore, to make clear the mechanism to form low resistivity in shale gas reservoirs, the matrix resistivity was calculated through the percolation network simulation based on pore structure characteristics and mineral compositional parameters. Moreover, the resistivity in low-resistivity laminations of shale was measured through the finite element simulation. In addition, the reasons for such low resistivity in shale were analyzed according to the resistivity-forming mechanism, and the effects of penetration degree, width, quantity, and spatial distribution of the laminations on the resistivity were worked out. Those may provide theoretical support for explaining the phenomenon of low-resistivity gas reservoirs.

1. Introduction

A success of shale gas in North America started a "shale revolution" all over the world. In China, a strategic breakthrough on shale gas has also been made along with the sustained progress in exploration and development technologies [1–6]. In fact, China has the largest technically recoverable reserves in the world, and Sichuan Basin possesses the most abundant shale gas resources in China [7–14]. And thus, shale gas has become one of the five high-end and growing industries developed in Sichuan Province.

Fluid saturation is one of the vital factors on the gas reserves in shale [15, 16], and resistivity is one of the crucial parameters for saturation evaluation during well logging, reservoir classification, and reserve calculation [17–19]. Oil and gas reservoirs are often characterized by high resistivity whereas water layers by low resistivity. However, in some shale reservoirs, the resistivity is low. According to the literatures [20–28], whether in Changning-Weiyuan and Jiaoshiba

blocks in Sichuan Basin, Cengong of Guizhou and Qinling-Qilian-Kunlun blocks in China, or the Barents Continental Shelf, or the Abi region of Nigeria, there are numerous shale gas reservoirs with low resistivity, with the lowest being $2.3\,\Omega\cdot m$, and even for some hydrocarbon-saturated ones, the resistivity ranges between $3.6\,\Omega\cdot m$ and $5.3\,\Omega\cdot m$, bringing about a great challenge to the evaluation of saturation through logging interpretation. According to the logging interpretation of certain shale strata in N11 in the western Sichuan Basin by an international logging company, both deep and shallow laterologs showed a resistivity of less than $10\,\Omega\cdot m$, indicating that the water saturation was over 70% and that the strata were not suitable for producing gas. However, the field saturation test in the same strata conducted by PetroChina Southwest Oil & Gasfield Company showed that the average saturation was only 29%. The well test conducted from April to May in 2013 showed a gas production of $0.77 \times 10^4\,m^3/d$, which also verified that these shale strata are gas reservoirs. Therefore, low resistivity

should no longer be taken as the principal evidence to ascertain whether there is water in shale reservoirs.

Quite a few scholars attempted to explain the reason of low resistivity in shale reservoirs. However, most of them focused on the qualitative analysis of statistics. Based on logging interpretation data, Yang et al. [29] summarized five key features of low-resistivity shale reservoirs, such as high clay content, high formation-water salinity, high organic maturity, high pyrite content, and high lamellation. Xie et al. [30] suggested that overmature organic matter, irreducible water, and thin interbed should be the main factors contributing to the low resistivity and that it was the graphite with strong conductivity in marine shale reservoirs that resulted in the resistivity decline. Passey et al. [31] affirmed that in overmature shale reservoirs, a certain carbonized kerogen also could lead to this decline. Based on the polarization and fluorescence thin-section identification results of some shale in both Qiongzhusi and Longmaxi formations, Sichuan Basin, Kethireddy et al. [32] and Sun et al. [33] proved the above results. Several studies [34, 35] put forward that not all organic matter in shale had been graphitized and that graphitization mostly relied on thermal evolution. Wang et al. [36] and Jiang et al. [37] summarized the graphitization features of the organic matter in these two formations and obtained the lower limit of graphitization R_o (3.5%) from Raman spectra, which was also verified by Hou et al. [38]. Beyond that, Zhao et al. [39] proposed graphite occurrence just standing for a higher level of organic carbonization.

Other scholars [24, 40–42] analyzed both formation water salinity and pyrite content based on logging and experimental data. Nevertheless, few network models have been established for numerical simulation of various factors. Most shale gas reservoirs are featured by apparent anisotropy owing to their complicated pore structure [43–47]; furthermore, the existence of conductive substances makes the conductive mechanism extremely complex, leading to difficulties in the application of the Archie equation which is commonly used for logging interpretation. Quite a few resistivity studies focused on conventional gas reservoirs, while few models incorporating pore structure features have been established for qualitative analysis. Therefore, with shale gas reservoirs as an example, the mechanism to form low resistivity was explored through numerical simulation and experiments on anisotropic resistivity.

Using the established network model to describe the features of both pore structure and spatial pattern of minerals can not only satisfy the pore structure features such as the size distribution of matrix pores on the microscopic level but also incorporate the distribution of overmature organic matter, pyrite, and fractures on the macroscopic level into the numerical simulation technologies of rock resistivity.

2. Pore Structure Features and Mineral Compositional Parameters in Shale

With the samples from Longmaxi Formation in H2 as an example, according to the analysis data of common minerals in rocks tested by the BRUKER Discovery 8 X-ray diffractometer, the mass fraction of pyrite in the crystal material is between 0.8% and 17.1%, with an average value of 3.97%. If calculated by the pyrite and rock densities of 4.91-5.27 g/cm^3 and 2.56-2.72 g/cm^3, respectively, the pyrite was just lower than 2.04% on average after the mass fraction was converted to a spatial pattern. The results from QEMSCAN are coincident with those from the X-ray diffraction.

The above experimental analysis can well obtain the spatial distribution characteristics of inorganic minerals and provide a reference for numerical simulation of resistivity. However, there is no reasonable method to explain the spatial distribution of organic matter. TOC fraction might only be clear after organic carbon analysis. According to some analysis on organic carbon in N11, this fraction varies from 1.18% to 8.44%, with an average of 2.71%. In addition, based on the organic-carbon and shale densities of 1.80 g/cm^3 and 2.46-2.67 g/cm^3, the estimated spatial fraction of organic carbon was in the range of 1.61% to 12.03%, with an average of 3.82%. After X-ray diffraction on the samples from this well, the obtained quartz fraction was between 34.6% and 90%, with an average of 51.5%, whereas the pyrite from 1.3% to 4.3%, with an average of 2.35%. The mineral composition in well N11 is similar to that in well H2.

3. Methodology

The percolation network model to describe the matrix pore structure has been widely used for the numerical simulation of reservoir rocks. Zhao et al. [48] conducted a quantitative study on the effects of porosity and clay and pyrite contents on the resistivity based on this model using the overrelaxation iterative method to solve the node voltage. They also tried to modify the Archie equation without considering the resistivity decline inferred from overmature organic matter. Tang [49] used this model to successfully simulate both single porous medium and resistivity transmission in fractured rocks. He et al. [19] modeled the resistivity in porous vuggy carbonate reservoir rocks by using the finite element method to obtain the matrix resistivity. In general, the percolation network model may present pore structure features such as pore diameter distribution and coordination number and reflect the true pore structure as much as possible.

3.1. Numerical Simulation Methods. Overmature organic matter, pyrite, lamination with formation water membranes, and fractures that are often common in shale are featured by better conductivity. Their conductive mechanism is realized by the conduction of free electrons and solution ions. However, the conductivities of graphite, natural pyrite, and brine with a salinity of 50g/L are $(8 \sim 15) \times 10^{-6}$ $\Omega \cdot$m [50], $10^{-3} \sim 1$ $\Omega \cdot$m [51], and 0.14 $\Omega \cdot$m, individually. Macroscopically, compared to the matrix, the above three materials are better conductors, while in the matrix, there are still common minerals with a conductivity of over 10^6 $\Omega \cdot$m, like calcite, feldspar, quartz, and mica. Like sandstone and carbonate rocks, the conduction of the shale matrix without low-resistivity substances depends on a connected network formed by formation water in pore structures. In terms of numerical simulation, shale can be subdivided into matrix and low-resistivity laminations for better understanding. The so-

called low-resistivity lamination means a certain zone where there developed overmature organic matter, pyrite, and fractures with formation-water membranes.

As for the numerical simulation of the matrix resistivity through the percolation network model, Bernabé et al. [52, 53] adopted 2D and 3D models to implement a numerical simulation of resistivity in a single porous medium. Li et al. [54] proposed a Li-Bernabé-Tang (LBT) model for calculating the matrix resistivity. Unlike conventional percolation network models, the resistivity of shale reservoir rocks was simulated in this study with the effects of low-resistivity lamination taken into consideration. Only when the lamination fraction accounts to 0 percent will the resistivity model be reduced to an absolute percolation network for a single porous medium. Two kinds of numerical simulation of the resistivity have certain unanimous views, one for rocks at the low-resistivity lamination and another in fractured or vuggy reservoirs.

The numerical simulation of the resistivity in fractured reservoirs with various fracture geometries [6, 55–57] is more complicated than that in a single porous medium. However, most of the simulations merely cared about regular and complete fractures without considering the spatial relations between fractures and the position of the fractures in the rock. Zhang [58] theoretically modeled the resistivity when fractures were fully saturated with water or oil and then analyzed the matrix and formation water resistivities as well as fracture dips, without taking into account the complexity of fracture penetration. In low-resistivity laminations, fractures are developed with formation water membranes, and the distribution pattern of both pyrite and overmature organic matter is similar to the fracture occurrence. Consequently, the numerical simulation for fractured reservoir rocks may serve as a reference for analysis. To overcome the above difficulties, this paper carried out a numerical simulation of rock resistivity by taking into account framework, angles, and distribution characteristics of "low-resistance laminations." According to the electric potential field theory, the electric potential field pattern in the reservoir rock can be described by the following equations:

$$\nabla \cdot \mathbf{J} = Q_{j,v},$$
$$\mathbf{J} = \sigma \mathbf{E} + \mathbf{J}_e, \qquad (1)$$
$$\mathbf{E} = -\nabla U.$$

The current density in the 2D rectangular coordinated system is as follows:

$$\mathbf{J} = \mathbf{i}J_x + \mathbf{j}J_y. \qquad (2)$$

The divergence of current density is as follows:

$$\nabla \cdot \mathbf{J} = \frac{\partial J_x}{\partial x} + \frac{\partial J_y}{\partial y}. \qquad (3)$$
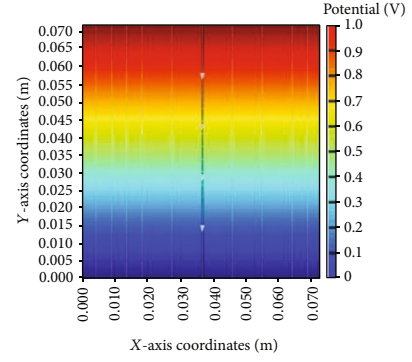

Figure 1: Simulation of potential distribution when low-resistivity lamination penetrates rocks. In general, the percolation network model may present pore structure features such as pore diameter distribution and coordination number and reflect the true pore structure as much as possible.
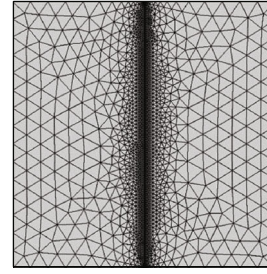

Figure 2: Schematic diagram of the finite element mesh model. He et al. [19] modeled the resistivity in porous vuggy carbonate reservoir rocks by using the finite element method to obtain the matrix resistivity.

The electric field intensity is as follows:

$$E = \mathbf{i}E_x + \mathbf{j}E_y. \qquad (4)$$

The 2D vector-valued differential operator is expressed as follows:

$$\nabla = \frac{\mathbf{i}\partial}{\partial x} + \frac{\mathbf{j}\partial}{\partial y}. \qquad (5)$$

On the basis of various lamination frameworks, a finite element simulation model was developed to acquire the potential field pattern in shale reservoir rocks (Figure 1). In addition, Figure 2 exhibits one pattern within a square with a side length of 0.07 m, a potential of 1 V at the square top and 0 V at the bottom, and both square sides under the periodical boundary condition.

$$U(0, y) = U(x_0, y). \qquad (6)$$

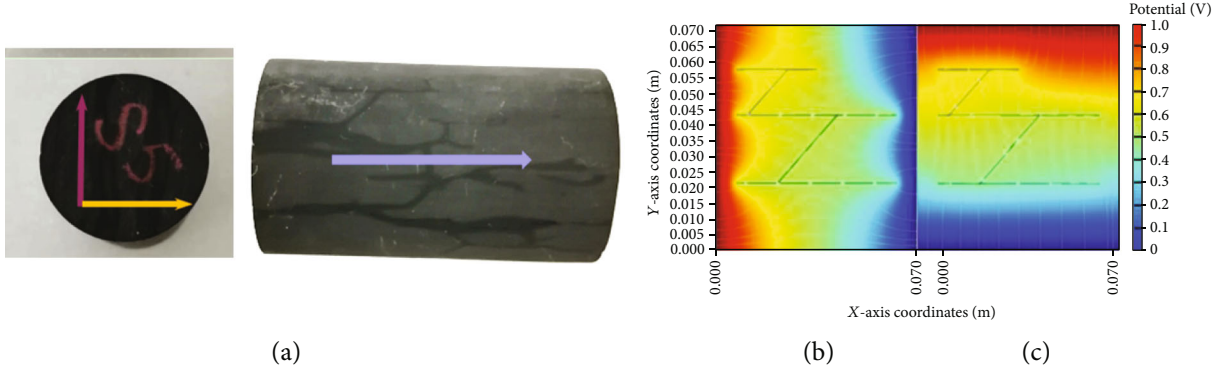(a)

(b)   (c)

FIGURE 3: Resistivity of shale sample verified by test and numerical simulation: (a) core sample S5, (b) lamination in parallel with the current direction, and (c) lamination vertical to the current direction. (a) The shale sample S5 was selected for experimental testing [59]. (a) Shows the axial lamination of the sample. (b) The numerically simulated value of resistivity in the parallel lamination was 67.39 $\Omega \cdot$m. (c) That in the vertical lamination was 108.70 $\Omega \cdot$m. The numerical simulation results are in good agreement with the measured core results.

The current density on the boundary is calculated from Equations (7) to (8).

$$J_{y,\text{input}} = \sum_{i=1}^{n} \sigma^{i,1} E_y^{i,1} - \sum_{i=1}^{n} \sigma^{i,0} E_y^{i,0}, \tag{7}$$

$$J_{y,\text{output}} = \sum_{i=1}^{n} \sigma^{i,n+1} E_y^{i,n+1} - \sum_{i=1}^{n} \sigma^{i,n} E_y^{i,n}. \tag{8}$$

In accordance with the principle of conservation of current, that $J_{y,\text{input}}$ equals $J_{y,\text{output}}$ just manifests a stable potential distribution. The resistivity is calculated by the following equation:

$$\rho = \frac{1}{\sigma} = \frac{E_y}{J_y}. \tag{9}$$

3.2. Examples of Application. To verify the effectiveness of the above numerical simulation method for resistivity, the shale sample S5 was selected for experimental testing [59]. Figure 3(a) shows the axial lamination of the sample. After S5 was fully saturated by brine with a salinity of 30 g/L, the radial resistivity in the parallel and vertical laminations was 65.65 $\Omega \cdot$m and 112.2 $\Omega \cdot$m, respectively. Therefore, according to the lamination framework, one numerical simulation model was built, setting the matrix resistivity at 146 $\Omega \cdot$m and the formation water resistivity at 0.2707 $\Omega \cdot$m. The numerical simulation was carried out using the method described above. As shown in Figures 3(b) and 3(c), the numerically simulated value of resistivity in the parallel lamination was 67.39 $\Omega \cdot$m, and that in the vertical lamina-tion was 108.70 $\Omega \cdot$m. The deviations between the numeri-cally simulations of core radial resistivity and the test results were 2.58% and 3.21%, both less than 5%. Appar-ently, the above method applied in the numerical simula-tion of resistivity can reflect the actual resistivity features of rocks.

Through the numerical simulation, the relations of various frameworks and spatial distributions of the low-resistivity laminations with the resistivity can be acquired.

4. Discussion

There are many influential factors on resistivity. In this study, those parameters close to the actual formation condi-tions were numerically simulated to reflect the effects of various factors to the greatest extent. To characterize the relations between the low-resistivity lamination and resistiv-ity, both the matrix and lamination resistivities were assumed at 100 $\Omega \cdot$m and 0.1 $\Omega \cdot$m, individually. According to the research of Xiao et al. [60], when the salinity of salt water is high, the influence of surface conductivity is very small. Therefore, the additional conductivity of clay is not specially considered in the simulation.

After a few experiments on samples from well N3, it was found that the resistivity under different saturations varied from 11.35 $\Omega \cdot$m to 355.58 $\Omega \cdot$m in those samples from the same horizon at a similar well depth and with a similar pore structure. For some of them, the rock resistivity ranged from 114.6 $\Omega \cdot$m to 124.4 $\Omega \cdot$m, while the samples were 100% satu-rated by some brine with a resistivity of 0.1273 $\Omega \cdot$m. Since shale is tight, the water saturation cannot decrease in the process of gas driving water. Therefore, it is deemed that the resistivity at this time represents the matrix resistivity in shale saturated by 100% brine. The matrix resistivity was assumed at 100 $\Omega \cdot$m in this simulation.

Figure 4(b) exhibits a little lamina developed in shale res-ervoirs. Moreover, the core observation indicates that there are overmature organic matters in the form of carbonized mirror plane. Thus, the low-resistivity lamination in this numerical simulation is used to describe a certain zone where there developed overmature organic matter, pyrite, and fractures on formation water membranes. The resistivity of brine with a salinity of 10 g/L is 0.1206 $\Omega \cdot$m, whereas the resistivity of high-salinity brine, pyrite, and graphite is below 0.1206 $\Omega \cdot$m. The purpose of this study is to demonstrate the mechanism of resistivity decline in both the high-resistivity
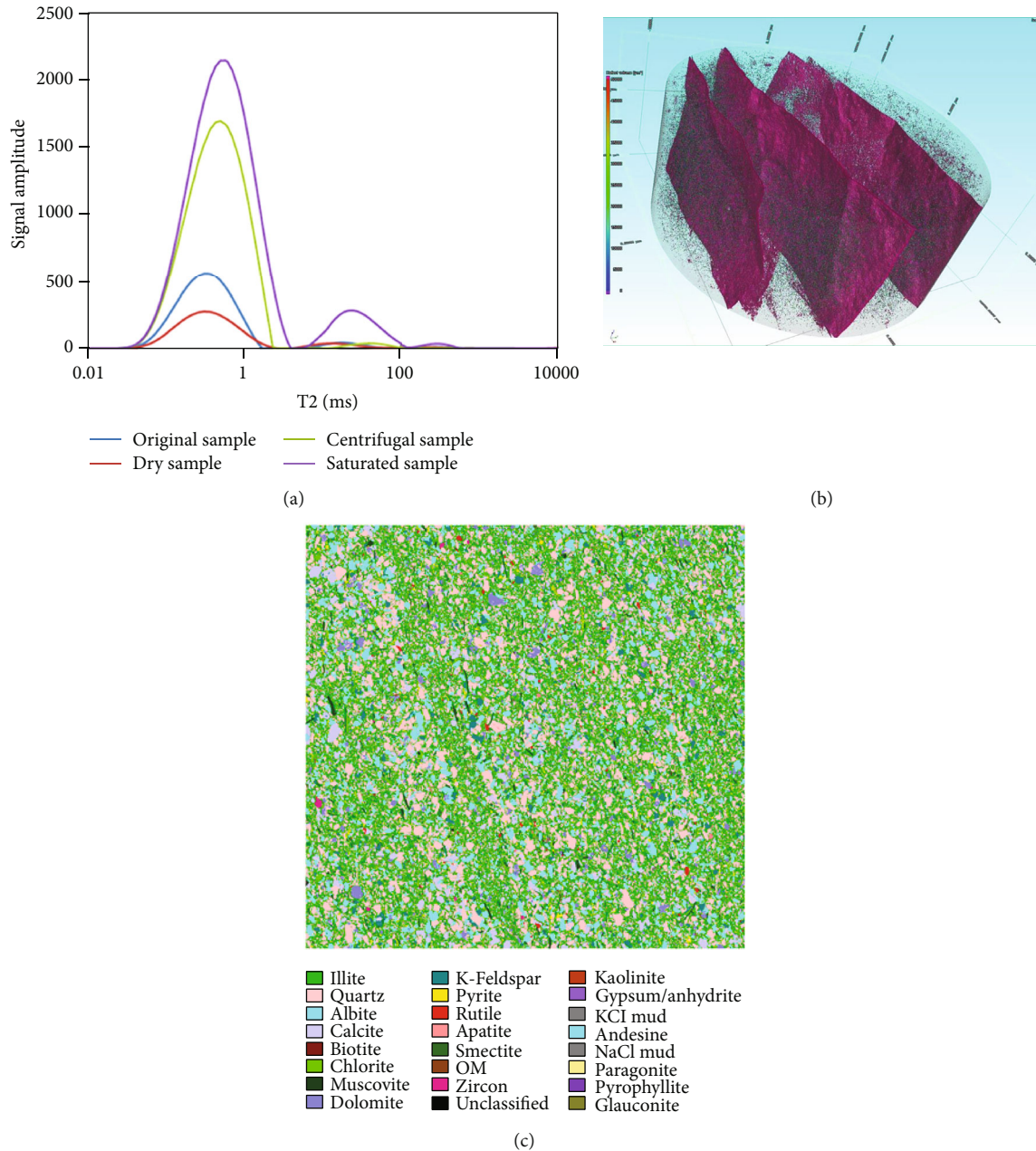
(a)

(b)

(c)

FIGURE 4: Extraction of characteristic parameters of shale pore structure, including (a) core T2 diagram from NMR scanning, (b) core photo from CT scanning, and (c) mineral distribution diagram (size: 3 mm × 3 mm; pixel: 1 μm). (a) Some representative samples from Longmaxi Formation in Changning-Weiyuan National Demonstration Area, Sichuan Basin, were analyzed by the core displacement apparatus MeoMR23-060H-I NMR manufactured by Suzhou Niumag Analytical Instrument Corporation in China to determine the pore diameter distribution. (b) A bimodal shape can be apparently seen in (a) whereas laminations from GE Phoenix X-ray CT scan in (b). On the whole, the lamination with obvious orientation is mutually complementary with the results from the NMR T2 spectroscopy. (c) A quantitative evaluation of minerals by scanning electron microscopy (QEMSCAN) demonstrated that pyrite presenting a discontinuously massive extension, amounting 1.61% of the total area (c).

matrix and the low-resistivity lamination on the macroscopic level through numerical simulation. Therefore, assigning the relatively high brine resistivity value to the resistivity of pyrite and overmature organic matter contributes a lot to making clear the low-resistivity mechanism in shale. Consequently, the lamination resistivity was assumed at 0.1 Ω·m in this simulation.

Through the simulation, the matrix resistivity of 100 Ω·m was compared with the lamination resistivity of 0.1 Ω·m in the shale at various phases and geometrical features.

4.1. Penetration Degree. Suppose the lamination is 0.00035 m wide and 0.07 m long and happens to penetrate the rock.
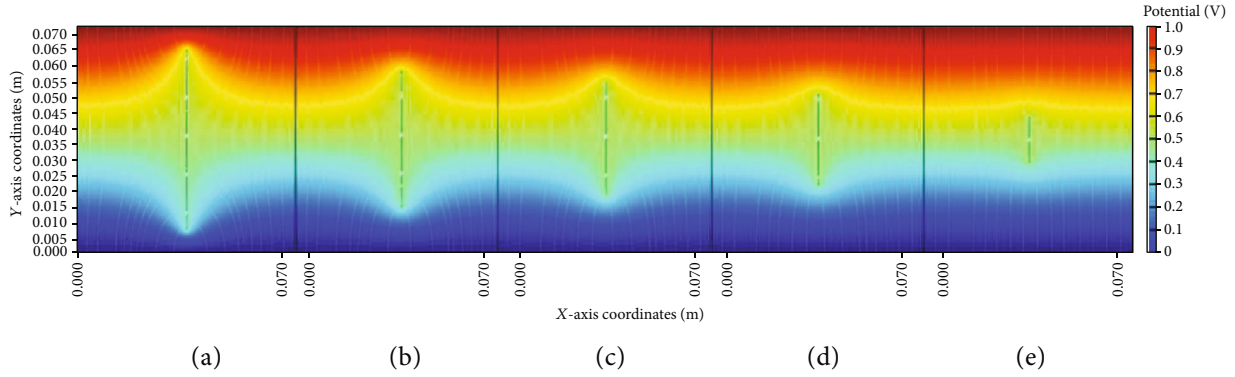
FIGURE 5: Potential distribution when the low-resistivity lamination does not penetrate rocks: various lamination lengths of (a) 0.056 m, (b) 0.042 m, (c) 0.035 m, (d) 0.028 m, and (e) 0.014 m.
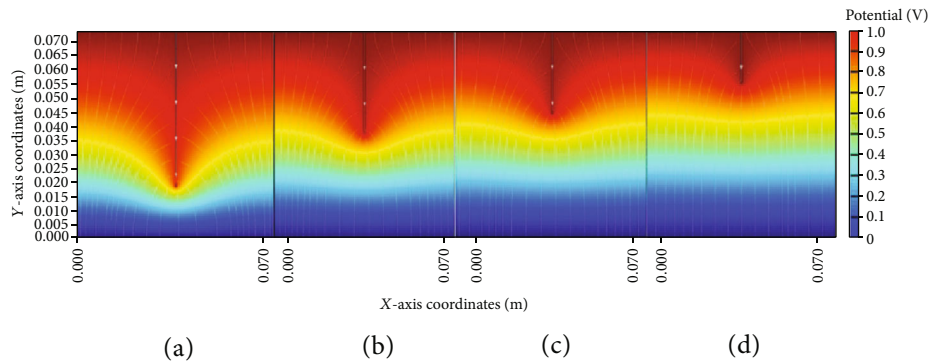

FIGURE 6: Potential distribution when low-resistivity lamination is semipenetrating rocks: various lamination lengths of (a) 0.0525 m, (b) 0.035 m, (c) 0.028 m, and (d) 0.0175 m.
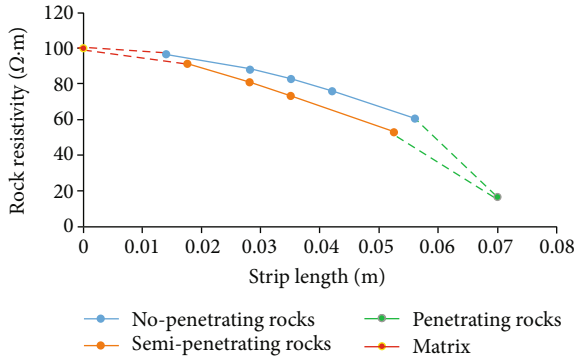

FIGURE 7: Effect of lamination length on rock resistivity. In the low-resistivity lamination, when the semipenetration area only accounts for 0.38%, the rock resistivity at the matrix resistivity of $100\,\Omega\cdot m$ drops to 53.2% of the origin matrix resistivity, which is $53.2\,\Omega\cdot m$. Moreover in this lamination, when the full penetration area accounts for 0.5%, the rock resistivity at the matrix resistivity of $100\,\Omega\cdot m$ drops to $16.68\,\Omega\cdot m$. The simulation verifies that the lamination greatly affects the resistivity even if the penetration area is extremely small.

Through the finite element numerical simulation previously described, the rock resistivity is calculated to be $16.68\,\Omega\cdot m$ in the Y axis. Thus, as the lamination penetrates the study area,

the resistivity can be reduced by more than 80% compared to the matrix resistivity of $100\,\Omega\cdot m$.

Supposing the lamination is disconnected on both sides, when the lamination has a width of 0.00035 m and a length of 0.056 m, 0.042 m, 0.035 m, 0.028 m, and 0.014 m, the corresponding resistivity is $60.70\,\Omega\cdot m$, $76.22\,\Omega\cdot m$, $82.67\,\Omega\cdot m$, $88.35\,\Omega\cdot m$, and $96.75\,\Omega\cdot m$. Figure 5 displays the spatial position of the lamination and the numerically simulated potential field.

Supposing that the lamination is connected with one rock side, when the lamination has a width of 0.00035 m and a length of 0.0525 m, 0.035 m, 0.028 m, and 0.0175 m, the corresponding resistivity is $53.27\,\Omega\cdot m$, $73.59\,\Omega\cdot m$, $81.25\,\Omega\cdot m$, and $91.46\,\Omega\cdot m$. Figure 6 shows the spatial position of the lamination and the numerically simulated potential field.

As shown in Figure 7, by comparing the three situations where the lamination penetrates, partially penetrates, or does not penetrate the rock, the resistivity is the lowest when the lamination fully penetrates the rock, followed by the resistivity when the lamination partially penetrates it and then that when the lamination does not penetrate it. In the situation where the lamination does not penetrate the rock, the resistivity even with the area fraction being 0.4% and the length being 0.056 m is higher than that with the area fraction being 0.38% and the length being 0.0525 m when
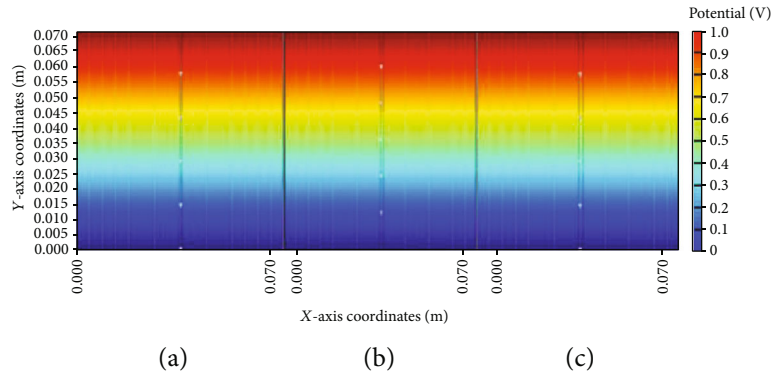
FIGURE 8: Potential distribution when the low-resistivity lamination penetrates rocks: different lamination widths of (a) 0.0007 m, (b) 0.00105 m, and (c) 0.0014 m.
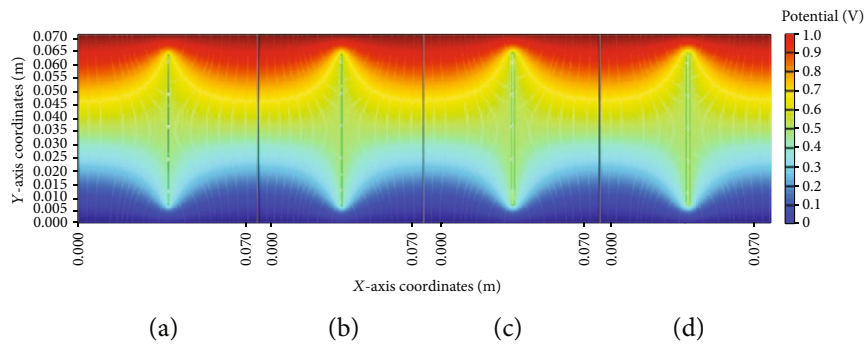

FIGURE 9: Potential distribution when the low-resistivity lamination does not penetrate the rock: at different lamination widths: (a) 0.00035 m, (b) 0.0007 m, (c) 0.00105 m, and (d) 0.00014 m.
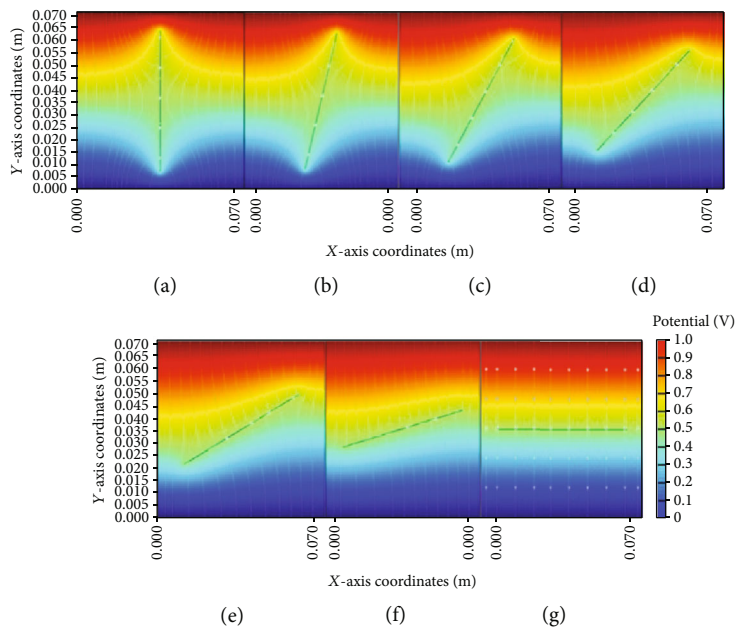

FIGURE 10: Potential distribution of the low-resistivity lamination at different angles of (a) 0°, (b) 15°, (c) 30°, (d) 45°, (e) 60°, (f) 75°, and (g) 90°.
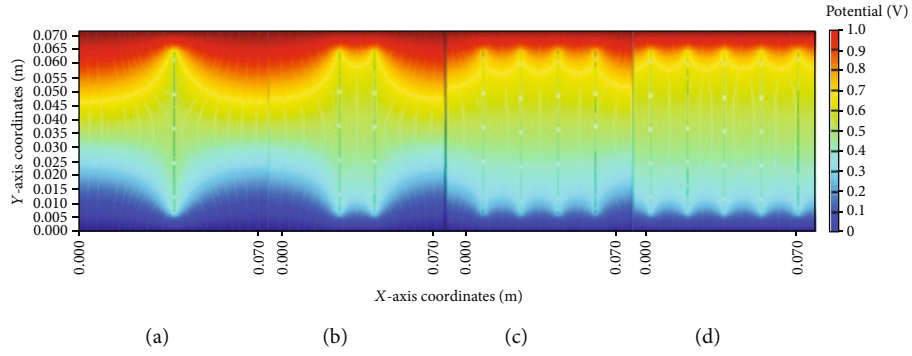
FIGURE 11: Potential distribution under different quantities of low-resistivity laminations with the same area fraction: (a) single lamination, (b) dual lamination, (c) four laminations, and (d) five laminations.
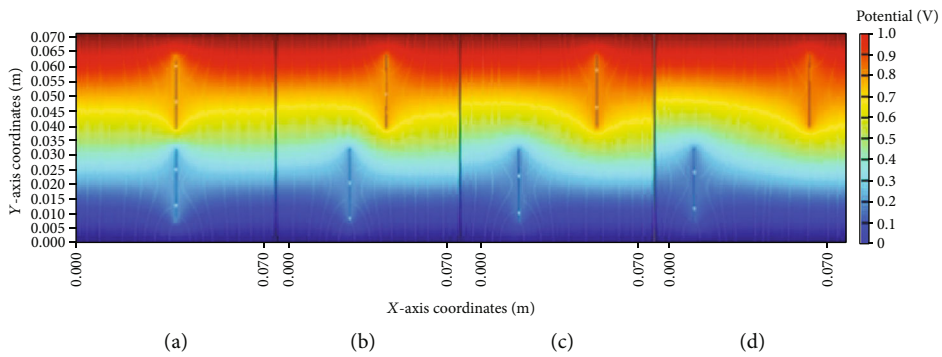

FIGURE 12: Potential distribution of the low-resistivity laminations with the same area fraction but different horizontal distances: (a) 0 m, (b) 0.014 m, (c) 0.028 m, and (d) 0.042 m.
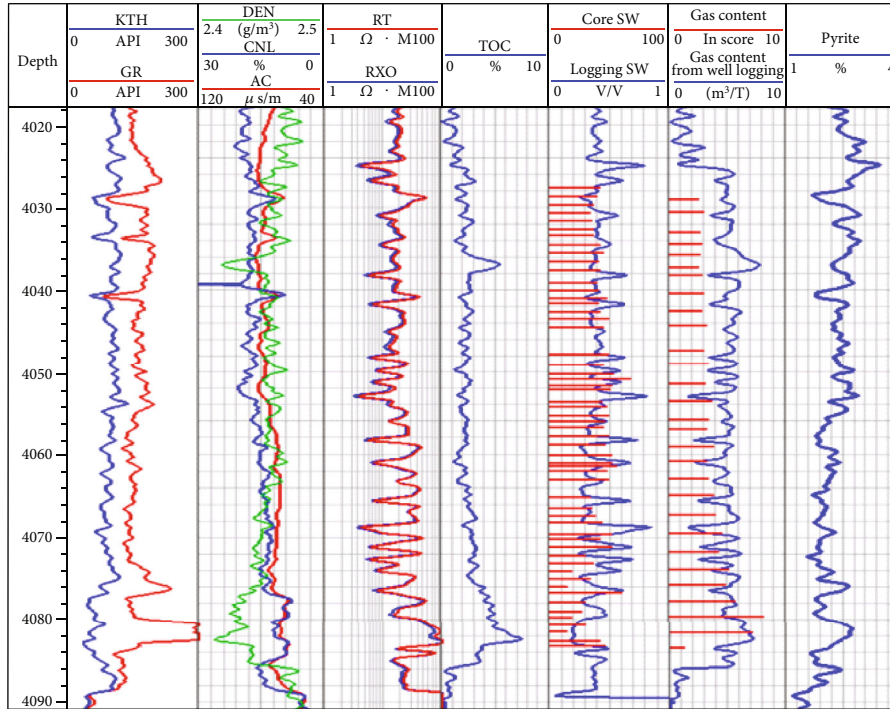

FIGURE 13: Logging curve of H2. A sharp decline inferred from some laminated pyrite is displayed. From the logging curves, not only the resistivity but also the corresponding density shows the shape of a spine. The density of the shale with pyrite is greater than that of the pyrite-free shale.
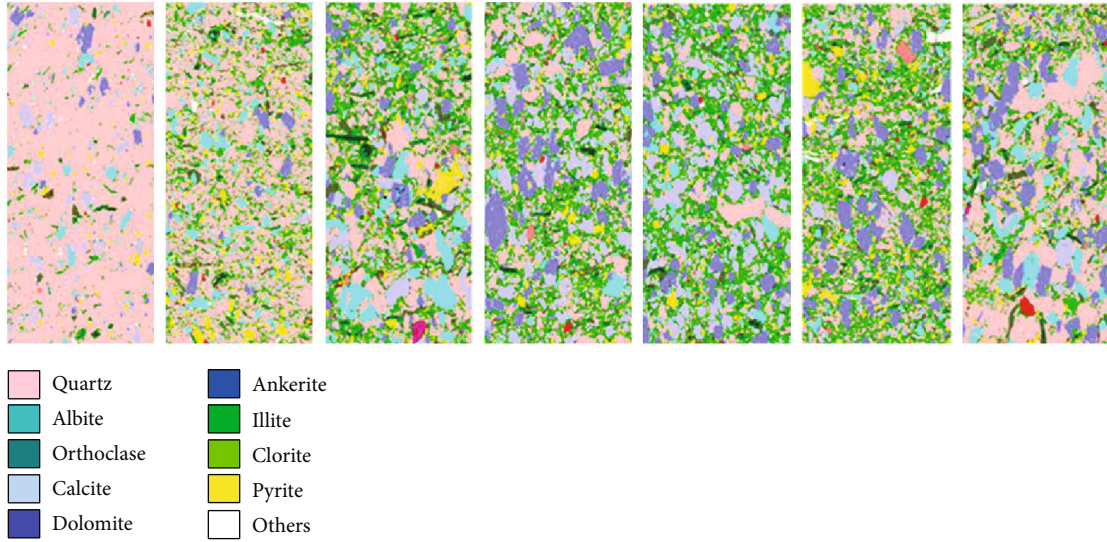
FIGURE 14: Pyrite distribution in QEMSCAN diagram. A qualitative mineral analysis was performed for samples from both wells N1 and W4-10-2 by a scanning electron microscope (SEM). However, SEM can identify common minerals except overmature organic matters. Like isolated islands, pyrite can be found in nonconductive common minerals, but the isolated pyrite makes no real difference in resistivity. This is very similar to the effect of rock resistivity of carbonate reservoirs with isolated vugs, and He et al. [19] give similar numerical simulation results about isolated shapes.

TABLE 1: Data on rock resistivity test of No. 4 sample from N24 well.

No.	Water saturation (%)	Rock resistivity ($\Omega\cdot$m)	Resistivity scaling coefficient
1	100	23.8	1.00
2	90.9	27.7	1.16
3	82.1	34.7	1.46
4	66.8	48.8	2.05
5	59.3	57.1	2.40
6	53.3	78.0	3.28
7	48.5	100.0	4.20
8	42.6	124.8	4.44

the lamination partially penetrates the rock. Therefore, a lower resistivity value does not signify a larger lamination whereas it relates to the position where the lamination is located.

4.2. Lamination Length. Setting the lamination penetrating rock as well as the lamination lengths at 0.0007 m, 0.00105 m, and 0.0014 m, the corresponding resistivity was calculated to be 9.10 $\Omega\cdot$m, 6.26 $\Omega\cdot$m, and 4.76 $\Omega\cdot$m. Figure 8 shows the simulated potential field. In the situation where the lamination penetrates the rock, its total area and width are, respectively, 0.0049 m^2 and 0.0014 m, and the area of the lamination only amounts to 2%; in other words, only a smaller part of the whole rock may lead to the resistivity declining to 4.8% of the matrix resistivity.

As shown in Figure 9, supposing that the lamination does not penetrate the rock, when the lamination has a length of 0.056 m and a width of 0.00035 m, 0.00007 m, 0.000105 m, and 0.00014 m, the corresponding resistivity was calculated to be 60.70 $\Omega\cdot$m, 57.79 $\Omega\cdot$m, 56.27 $\Omega\cdot$m, and 55.20 $\Omega\cdot$m. This also indicates that, if the lamination does not penetrate the rock, there is no notable change in the rock resistivity, and the area fraction of 1.6% may only bring about a resistivity decline to 55.2% of the matrix resistivity.

4.3. Angle between Current Flow and Low-Resistivity Lamination. To find the relationship of the angle between the current flow and the low-resistivity lamination with the corresponding resistivity, the finite element numerical simulation was conducted when the angle was 0°, 15°, 30°, 45°, 60°, 75°, and 90°, and the resulting resistivity was 60.7 $\Omega\cdot$m, 63.12 $\Omega\cdot$m, 69.68 $\Omega\cdot$m, 79.20 $\Omega\cdot$m, 89.23 $\Omega\cdot$m, 96.85 $\Omega\cdot$m, and 99.60 $\Omega\cdot$m (Figure 10), which demonstrates different resistivities in diverse directions.

4.4. Lamination Quantity. Despite the same area fraction for each low-resistivity lamination, the rock resistivity represents a great difference because of different lamination locations and quantities. Supposing the stimulated area fraction is 0.4%, but that there are multiple laminations parallel to each other (Figure 11), the resistivity was 60.7 $\Omega\cdot$m, 51.24 $\Omega\cdot$m, 41.8 $\Omega\cdot$m, and 37.75 $\Omega\cdot$m corresponding to one lamination, two laminations, four laminations, and five laminations, respectively.

4.5. Location Relation of Two Parallel Laminations. Additionally, the resistivity of two parallel laminations with different horizontal distances was simulated. Supposing that each lamination has a width of 0.00035 m, the resistivity was individually 73.29 $\Omega\cdot$m, 75.08 $\Omega\cdot$m, 76.73 $\Omega\cdot$m, and 77.75 $\Omega\cdot$m corresponding to four different horizontal
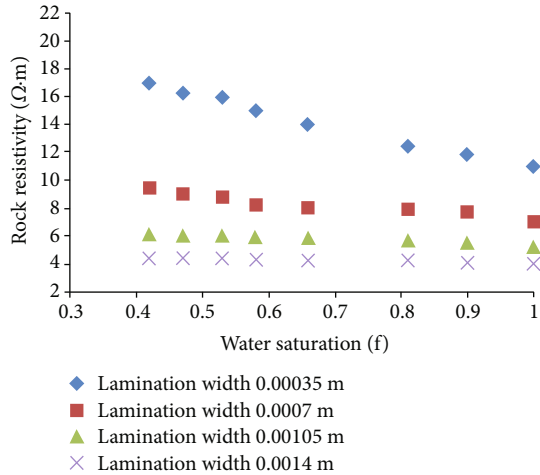
FIGURE 15: Relationship between water saturation and resistivity of shale penetrating low-resistivity lamination. It is observed that the water saturation in the rock matrix is no longer the main effect on the resistivity, and the functional relationship has been destructed by the lamination length. When the water saturation in the matrix pore is 40%, the rock resistivity in the low-resistivity lamination with different widths should be any resistivity from $5.0\,\Omega\cdot m$ to $18.0\,\Omega\cdot m$. Consequently, it is hard to identify the water saturation in shale only through the resistivity when the lamination framework cannot be predicted in advance.
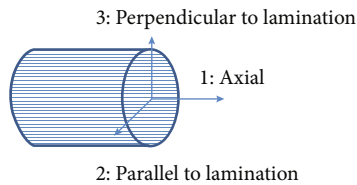

FIGURE 16: Schematic diagram of anisotropic resistivity test on shale with developed lamination: 1: end surface direction; 2: parallel to the lamination; 3: perpendicular to the lamination.

distances -0 m, 0.014 m, 0.028 m, and 0.042 m, as seen in Figure 12. It is not difficult to see that the increase of resistivity value is not evident when the distance between the two laminations enlarges.

Through the numerical simulation, the gained resistivities of rocks with different directions exist with a large diversity. Moreover, slightly conductive substances may considerably reduce the resistivity. Even a bit of pyrite and overmature organic matter can greatly affect the resistivity. Experiments also verify [59, 61] the anisotropic resistivity in shale and large resistivity discrepancy among rocks with different directions.

5. Results

Researchers have attempted to set up the functional relation between water saturation and resistivity and summarized that the formation water salinity, clay and pyrite contents, and overmature organic matter are the main factors contributing to the low resistivity in shale.
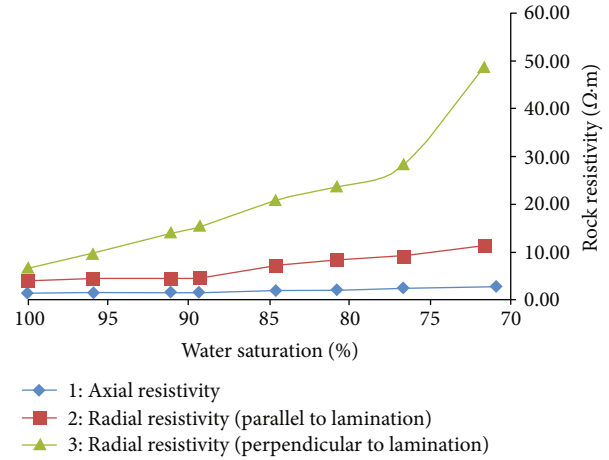

FIGURE 17: Anisotropic resistivity and water saturation of sample No. 10 from H6 well. The trend that the rock resistivity at different directions varies along with the water saturation is the same, whereas the variation degree is different. In pace with the decrease of water saturation, the resistivity perpendicular to the lamination may increase at a greater pace than that in other directions, especially for that parallel to the lamination where the increase is limited, which demonstrates that there are not enough conductive substances to create the connected network when the water saturation drops perpendicular to the lamination. As the saturation drops to 70%, the resistivity perpendicular to the lamination increases by five times as compared to that parallel to the lamination. For some samples with 100% water saturation, the resistivity in different directions is all below $10\,\Omega\cdot m$, indicating that this conductive network contains good conductors in all directions.
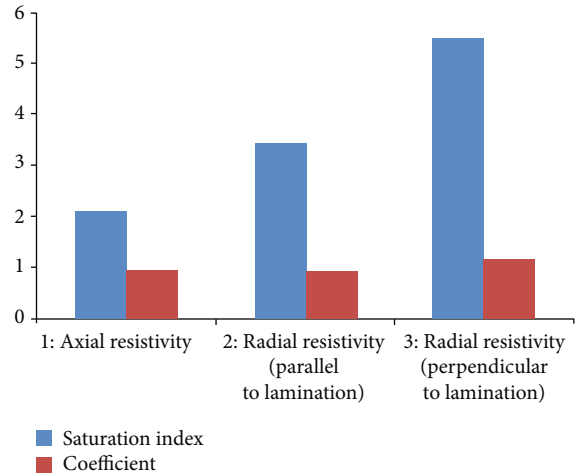
FIGURE 18: Variation law of resistivity, saturation index, and coefficient of sample No. 10 from H6. The saturation index changes greatly with different directions, and the coefficient changes little with different directions.

Previous experiments [62] proved that, when salinity increases to some extent, the effect is limited to the resistivity decline in brine, which means there is no reduction in the order of magnitude. Other scholars thought that rich clay
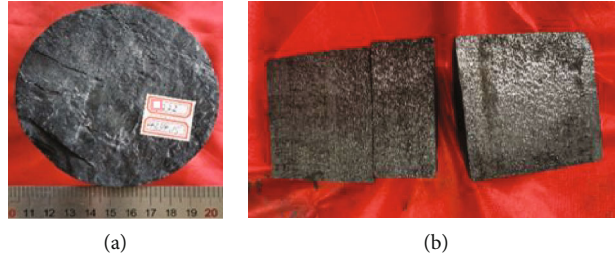
(a) (b)

FIGURE 19: Carbonized mirror plane exhibited in the organic matter of cores from (a) N22 and (b) N19. Some overmature organic matter just developed in the form of a carbonized mirror plane.

in shale reservoirs might also lead to resistivity decline, which is essentially because of the higher water saturation in the pores of the rocks which contain a high content of clay. Thus, formation water is the key factor. Dry clay and formation water are just like an insulator and a conductor.

5.1. Pyrite Content. Pyrite is also deemed as an important resistivity decline cause. The logging curve of H2 is shown in Figure 13.

As seen in the full-diameter cores from H2, there are some pyrites shown in the massive or ribbon form. It was found through the whole rock analysis based on X-ray diffraction that, owing to strong heterogeneity, the pyrite accounted for 0.18~17.1% of the crystalline minerals in terms of mass. However, it only accounted for 0.5~1% per the thin-section identification report of H2. At 100% formation water saturation, the rock resistivity ranged from 13.44 Ω·m to 61.48 Ω·m, but the corresponding pyrite accounted for the 3.1% of crystalline minerals, showing that pyrite content is not the only factor affecting the low resistivity. The QEMSCAN diagram of H2 is shown in Figure 14.

5.2. Water Saturation in Matrix. Some shale without conductive substances at the low-resistivity lamination accords with the assumption of the Archie equation. For sample No. 4 from Longmaxi Formation in N24, the porosity, water-saturated salinity, and brine resistivity are 2.53%, 29 g/L, and 0.3023 Ω·m, respectively. Table 1 lists some experimental data received from RCCP-301 apparatus manufactured by CoreLab Company. The rock resistivity increases to 124.8 Ω·m from 23.8 Ω·m along with the water saturation decreasing to 42.6% from 100%. And this trend conforms to the resistivity change law in porous reservoir rocks without the developed low-resistivity lamination.

Moreover, the trend may be destructed because of the low-resistivity lamination. Supposing this sample was being penetrated by one lamination (Figures 1 and 8), the relationship between rock resistivity with different lamination widths and water saturation can be figured out by the numerical simulation (Figure 15).

5.3. Fracture. From the numerical simulation, the lamination penetrating rocks may result in the sharp resistivity decline. Fractures with formation water are also involved in the context of low-resistivity lamination. In 2020, He et al. [59] developed an experimental method on the radial resistivity

TABLE 2: Logging resistivity, experimental TOC, and water saturation.

Well	Resistivity (Ω·m)	TOC (%)	Water saturation (%)
N11	8.3	3.82	36.31
N19	0.20	3.60	65.37
N21	0.42	3.97	
N27	11		27.13
N28	0.43	1.36	69.74
N30	0.98	4.24	69.74
N31	0.21	5.05	73.29

characterizing plug anisotropy. The resistivity under different water saturations may be calculated by means of this method (Figure 16).

5.4. Overmature Organic Matter. As shown in Figure 17, the low-resistivity lamination containing fractures saturated with water may reduce the resistivity parallel to the lamination to 10 Ω·m. And the saturation index and coefficient of sample No. 10 from H6 are shown in Figure 18. However, this is not obviously all reason to form low resistivity in shale just because the resistivity perpendicular to the lamination is only 10 Ω·m at 100% formation water saturation, too. The resistivity of 10 Ω·m is not reduced by the penetration formed by water-bearing fractures. Therefore, other factors can also bring about low resistivity.

Figure 19 exhibits some overmature organic matter just developed in the form of a carbonized mirror plane. According to the analysis of organic carbon in N11, the organic carbon fraction is about between 1.61% and 12.03%, with an average of 3.82%. Deep and shallow laterlog shows that all resistivities in some reservoirs of N11 are less than 10 Ω·m. However, the gas production of 0.77×10^4 m^3/d can affirm that these reservoirs have economic value despite the resistivity being less than 10 Ω·m. As listed in Table 2, even if the water saturation is as low as 36.41%, the resistivity can still be less than 10 Ω·m as long as the organic carbon reaches a certain value.

Issued by CoreLab Company, the Fundamentals of Core Analysis point out that solution resistivity may decrease along with the salinity increasing. At the solution temperature of 23.89°C (75°F), when the salinity of the NaCl solution is 2 g/L, the resistivity is 4.6 Ω·m, when the salinity is 7 g/L,

the resistivity is reduced to $1\,\Omega\cdot m$; and when the salinity increases to $80\,g/L$, the resistivity is about $0.1\,\Omega\cdot m$. In physics, such material particles with charge and free movement as electrons and ions are called as carriers. In other words, the resistivity represents the ability of a material to hinder the free passage of carriers. In a sense, the resistivity at the same order of magnitude means that the material has an identical ability to impede the carriers to move. The solution conduction depends on ion movement, so the resistivity is, in a sense, a measure of the free passage of the carriers in the solution. When the salinity of saturated formation water is less than $2\,g/L\sim7\,g/L$, the shale resistivity is still smaller than $10\,\Omega\cdot m$. It is worth noting that the shale saturated with formation water is an aqueous porous media system, rather than as pure solution, which is also an evidence that the shale skeleton itself contains conductive substances. For example, for most of the shale samples from Y1 in the southern Sichuan Basin, the resistivity is lower than $5\,\Omega\cdot m$ after the samples are dried.

6. Conclusions

In this paper, based on lamination and mineral composition, the numerical simulation method for reservoir rock resistivity was used to analyze the reasons for the low resistivity of shale from the rock conductivity mechanism, which might provide a theoretical basis for explaining the low-resistivity gas reservoirs from logging interpretation. Moreover, as for the low-resistivity lamination, the penetration degree, width, quantity, and spatial pattern as well as the effect of current flow angle on the resistivity were summarized. In addition, the effects of pyrite content, fracture geometry, and overmature organic matter on the resistivity were explored one by one. Three conclusions are made as follows.

For some rocks containing low-resistivity laminations, the resistivity in different directions is diverse, and it may be reduced a lot by just a bit of continuous conductive substance.

Fracture geometry may significantly influence the resistivity anisotropy. And the resistivity may be reduced a lot by overmature organic matters that account for only 2% of the space.

From a great deal of experimental data and numerical simulation, it is proven that many conductive substances in shale may bring about challenges to making clear the relationship of resistivity with water saturation. High resistivity means gas can be produced, but different from conventional logging theory, low resistivity does not always mean that the shale strata are not gas reservoirs. Due to the existence of conductive substances such as overmature organic matter and pyrite, even if the resistivity is below $10\,\Omega\cdot m$, there is still gas-producing potential in these strata.

Nomenclature

Symbols

P: Resistivity ($\Omega\cdot m$)
φ: Porosity (%)
σ: Conductivity (S/m)
$\sigma_{i,j}$:   Conductivity of No. i at the X axis and No. j at the Y axis (S/m)
E: electric field intensity (V/m)
E_x: Electric field intensity component at the X axis (V/m)
E_y: Electric field intensity component at the Y axis (V/m)
$E_{i,j}$:   Electric field intensity at No. i at the X axis and No. j at the Y axis (V/m)
i: Unit vector of the X axis
j: Unit vector of the Y axis
J: Current density (A/m^2)
J_x: Current density component at the X axis (A/m^2)
J_y: Current density component at the Y axis (A/m^2)
$J_{y,\text{input}}$:   Current density component in the inlet at the Y axis (A/m^2)
$J_{y,\text{output}}$:   Current density component in the outlet at the Y axis (A/m^2)
J_e: Displacement current density (A/m^2)
$Q_{j,v}$:   Charge quantity per unit volume (C/m^3)
U: Voltage (V)
x_0:   Length of potential field at the X axis (m).

Data Availability

Data are available from the corresponding author on reasonable request.

Conflicts of Interest

The authors declare that there is no conflict of interest regarding the publication of this paper.

Acknowledgments

References

[1] J. H. He, "Will the prosperity of unconventional natural gas development in North America reappear in China?," *Advances in Energy Sciences*, vol. 4, no. 2, pp. 45–49, 2007.

[2] C. Shen, L. Ren, J. Z. Zhao, X. C. Tan, and L. Z. Wu, "A comprehensive evaluation index for shale reservoirs and its application: a case study of the Ordovician Wufeng Formation to Silurian Longmaxi Formation in southeastern margin of

Sichuan Basin, SW China," *Petroleum Exploration and Development*, vol. 44, no. 4, pp. 686–695, 2017.

[3] D. A. Wood, "Techniques used to calculate shale fractal dimensions involve uncertainties and imprecisions that require more careful consideration," *Advances in Geo-Energy Research*, vol. 5, no. 2, pp. 153–165, 2021.

[4] X. Jin, G. X. Li, S. W. Meng et al., "Microscale comprehensive evaluation of continental shale oil recoverability," *Petroleum Exploration and Development*, vol. 48, no. 1, pp. 222–232, 2021.

[5] J. Wu, T. Goto, and K. Koike, "Estimating fractured rock effective permeability using discrete fracture networks constrained by electrical resistivity data," *Engineering Geology*, vol. 289, article 106178, 2021.

[6] J. Wu, H. Y. Wang, Z. S. Shi et al., "Favorable lithofacies types and genesis of marine-continental transitional black shale: a case study of Permian Shanxi Formation in the eastern margin of Ordos Basin, NW China," *Petroleum Exploration and Development*, vol. 48, no. 6, pp. 1315–1328, 2021.

[7] J. H. He, N. Li, L. S. Wang, J. Zhang, J. Du, and T. Jin, "Automatic shale gas content measurement technology," *Oil Drilling & Production Technology*, vol. 39, no. 6, pp. 766–770, 2017.

[8] K. Li, S. Kong, P. Xia, and X. Wang, "Microstructural characterisation of organic matter pores in coal-measure shale," *Advances in Geo-Energy Research*, vol. 4, no. 4, pp. 372–391, 2020.

[9] X. Liang, Z. Y. Xu, Z. Zhang et al., "Breakthrough of shallow shale gas exploration in Taiyang anticline area and its significance for resource development in Zhaotong, Yunnan Province, China," *Petroleum Exploration and Development*, vol. 47, no. 1, pp. 12–29, 2020.

[10] X. H. Ma, J. Xie, R. Yong, and Y. Q. Zhu, "Geological characteristics and high production control factors of shale gas reservoirs in Silurian Longmaxi Formation, southern Sichuan Basin, SW China," *Petroleum Exploration and Development*, vol. 47, no. 5, pp. 901–915, 2020.

[11] Z. H. Xu, M. J. Zheng, Z. H. Liu et al., "Petrophysical properties of deep Longmaxi Formation shales in the southern Sichuan Basin, SW China," *Petroleum Exploration and Development*, vol. 47, no. 6, pp. 1100–1110, 2020.

[12] Y. H. Fu, Y. Q. Jiang, D. Z. Dong et al., "Microscopic pore-fracture configuration and gas-filled mechanism of shale reservoirs in the western Chongqing area, Sichuan Basin, China," *Petroleum Exploration and Development*, vol. 48, no. 5, pp. 1063–1076, 2021.

[13] X. He, W. G. Li, L. R. Dang et al., "Key technological challenges and research directions of deep shale gas development," *Natural Gas Industry*, vol. 41, no. 1, pp. 118–124, 2021.

[14] X. He, J. F. Wu, R. Yong et al., "Accumulation conditions and key exploration and development technologies of marine shale gas field in Changning-Weiyuan block, Sichuan Basin," *Acta Petrolei Sinica*, vol. 42, no. 2, pp. 259–272, 2021.

[15] L. J. Yan, X. X. Chen, H. Tang et al., "Continuous TDEM for monitoring shale hydraulic fracturing," *Applied Geophysics*, vol. 15, no. 1, pp. 26–34, 2018.

[16] B. Pan, A. Ruhan, Y. Guo, L. Zhang, B. Wei, and W. Zhou, "Study on the relationship between complex resistivity and water saturation in fractured rock at low frequency," *Chinese Journal of Geophysics*, vol. 64, no. 10, pp. 3774–3787, 2021.

[17] G. E. Archie, "The electrical resistivity log as an aid in determining some reservoir characteristics," *Transactions of AIME*, vol. 146, no. 1, pp. 54–62, 1942.

[18] J. G. Sun, "Archie's formula: historical background and earlier debates," *Progress in Geophysics*, vol. 22, no. 2, pp. 472–486, 2007.

[19] J. H. He, M. Li, K. M. Zhou et al., "Effects of vugs on resistivity of vuggy carbonate reservoirs," *Petroleum Exploration and Development*, vol. 47, no. 3, pp. 527–535, 2020.

[20] T. Zhu, J. Zhou, and J. Hao, "Resistivity anisotropy and its applications to earthquake research," *Progress in Geophysics*, vol. 24, pp. 871–878, 2009.

[21] D. E. Ebong, E. A. Anthony, and A. O. Anthony, "Estimation of geohydraulic parameters from fractured shales and sandstone aquifers of Abi (Nigeria) using electrical resistivity and hydrogeologic measurements," *Journal of African Earth Sciences*, vol. 96, pp. 99–109, 2014.

[22] J. S. He, D. Q. Li, and S. K. Dai, "Shale gas detection with wide field electromagnetic method in North-Western Hunan," *Oil Geophysical Prospecting.*, vol. 49, no. 5, pp. 1006–1012, 2014.

[23] K. Xiang, W. B. Hu, L. J. Yan, X. G. Tang, and X. B. Xie, "Shale gas reservoir characterization and geophysical prediction," *Special Oil and Gas Reservoir.*, vol. 23, no. 2, pp. 5–8, 2016.

[24] K. Xiang, L. J. Yan, H. Hu, W. B. Hu, X. G. Tang, and X. J. Liu, "Relationship analysis between brittle index and electrical properties of marine shale in South China," *Geophysical Prospecting for Petroleum.*, vol. 55, no. 6, pp. 894–903, 2016.

[25] L. Y. Zhang, S. R. Li, L. B. Wang, F. Chen, and B. Geng, "A new method for calculating gas saturation of low-resistivity shale gas reservoirs," *Natural Gas Industry B*, vol. 4, no. 5, pp. 346–353, 2017.

[26] F. Y. Meng, S. J. Bao, K. Chen, P. Wang, and L. D. Li, "The prediction of shale gas favorable area based on wide area electromagnetic method: a case study of Wushan area in northeast Chongqing," *Geophysical & Geochemical Exploration.*, vol. 42, no. 1, pp. 68–74, 2018.

[27] S. Kim, B. Thomas, B. Peter, O. S. Kei, O. Snorre, and S. P. Renate, "Resistivity of reservoir sandstones and organic rich shales on the Barents Shelf: implications for interpreting CSEM data," *Geoscience Frontiers*, vol. 12, pp. 1–17, 2021.

[28] Y. Z. Ma, "Comparative test of WFEM and AMT in the shale gas block of Babaoshan," *Geology of Chemical Minerals*, vol. 42, no. 4, pp. 334–347, 2020.

[29] X. B. Yang, S. D. Zhang, Z. G. Zhang, J. Liu, and X. Deng, "Logging interpretation and evaluation of low resistivity shale gas reservoirs," *Journal of Chengdu University of Technology (Science & Technology Edition).*, vol. 42, no. 6, pp. 692–699, 2015.

[30] X. G. Xie, B. Luo, L. X. Yin, H. Y. Liang, and Y. X. Li, "Influence factors of low resistiviyt shale gas reservoir," *Acta Geologica Sichuan.*, vol. 37, no. 3, pp. 433–437, 2017.

[31] Q. R. Passey, F. J. Moretti, J. B. Kulla, S. Creaney, and J. D. Stroud, "Practical models for organic richness from porosity and resistivity logs," *AAPG Bulletin*, vol. 74, no. 12, pp. 1777–1794, 1990.

[32] N. Kethireddy, H. Chen, and Z. Heidari, "Quantifying the effect of kerogen on resistivity measurements in organic-rich mud rocks," *Petrophysics*, vol. 55, no. 2, pp. 136–146, 2014.

[33] J. M. Sun, Z. Xiong, H. Luo, H. P. Zhang, and J. J. Zhu, "Mechanism analysis and logging evaluation of low resistivity in lower Paleozoic shale gas reservoirs of Yangtze region,"

Journal of China University of Petroleum., vol. 42, no. 5, pp. 47–56, 2018.

[34] D. A. Wood and B. Hazra, "Pyrolysis S2-peak characteristics of Raniganj shales (India) reflect complex combinations of kerogen kinetics and other processes related to different levels of thermal maturity," *Advances in Geo-Energy Research*, vol. 2, no. 4, pp. 343–368, 2018.

[35] Z. Gao, Y. Fan, Q. Xuan, and G. Zheng, "A review of shale pore structure evolution characteristics with increasing thermal maturities," *Advances in Geo-Energy Research*, vol. 4, no. 3, pp. 247–259, 2020.

[36] Y. M. Wang, X. J. Li, B. Chen et al., "Lower limit of thermal maturity for the carbonization of organic matter in marine shale and its exploration risk," *Petroleum Exploration and Development*, vol. 45, no. 3, pp. 402–411, 2018.

[37] S. Jiang, Y. M. Wang, S. Y. Wang et al., "Distribution prediction of graphitized organic matter areas in the lower Cambrian Qiongzhusi shale in the Central Sichuan paleo-uplift and its surrounding areas in the Sichuan Basin," *Natural Gas Industry*, vol. 38, no. 10, pp. 19–27, 2018.

[38] Y. G. Hou, K. P. Zhang, F. R. Wang et al., "Structural evolution of organic matter and implications for graphitization in overmature marine shales, south China," *Marine and Petroleum*, vol. 109, pp. 304–316, 2019.

[39] W. T. Zhao, T. Y. Jing, X. Xiong, B. Wu, and Y. Zhou, "Graphitization characteristics of organic matters in marine-facies shale," *Geological Science and Technology Information.*, vol. 37, no. 2, pp. 183–191, 2018.

[40] Y. Lei, F. Q. Wang, H. J. Liu, and J. F. Chen, "Study on relationship between lithology and electric logging of mud shale in Cheng 7 Member of Yanchang Formation in Ordos Basin," *Journal of Xi'an Shiyou University (Natural Science Edition).*, vol. 27, no. 2, pp. 27–35, 2012.

[41] Z. Q. Zhong, R. Rezaee, M. Josh, L. Esteban, and M. Sarmadivaleh, "The salinity dependence of electrical conductivity and Archie's cementation exponent in shale formations," *Journal of Petroleum Science and Engineering*, vol. 208, article 109324, 2022.

[42] P. Zhang, S. Lu, J. Li, J. Zhang, H. Xue, and C. Chen, "Permeability evaluation on oil-window shale based on hydraulic flow unit: a new approach," *Advances in Geo-Energy Research*, vol. 2, no. 1, pp. 1–13, 2018.

[43] X. Nie, C. C. Zou, X. H. Meng, S. Jia, and Y. Wan, "3D digital core modeling of shale gas reservoir rocks: a case study of conductivity model," *Natural Gas Geoscience*, vol. 27, no. 4, pp. 706–715, 2016.

[44] X. Nie, Y. Wan, and B. Fan, "Dual-shale-content method for total organic carbon content evaluation from wireline logs in organic shale," *Open Geoscience*, vol. 9, pp. 133–137, 2017.

[45] X. Kun, C. C. Zou, Z. Q. Lu, and J. Z. Deng, "Gas hydrate saturations estimated from pore-and fracture-filling gas hydrate reservoirs in the Qilian Mountain permafrost, China," *Scientific Reports*, vol. 7, no. 1, pp. 1–16, 2017.

[46] L. Q. Zhu, Y. S. Ma, J. C. Cai, C. M. Zhang, S. G. Wu, and X. Q. Zhou, "Key factors of marine shale conductivity in southern China—part II: theinfluence of pore system and the development direction of shale gas saturation models," *Journal of Petroleum Science and Engineering*, vol. 209, pp. 1–17, 2022.

[47] B. K. Li, X. Nie, J. C. Cai, X. Q. Zhou, C. C. Wang, and D. L. Han, "U-Net model for multi-component digital rock modeling of shales based on CT and QEMSCAN images," *Journal of Petroleum Science and Engineering*, vol. 216, pp. 1–14, 2022.

[48] J. Zhao, X. Y. Dai, Y. F. Lu, and S. H. Tang, "Shale reservoir conductive mechanism simulation based on percolation network," *Chinese Journal of Geophysics*, vol. 60, no. 5, pp. 2020–2028, 2017.

[49] Y. B. Tang, "Percolation network study on the electrical properties of rocks and applications", [Ph.D. Thesis], Southwest Petroleum University, Chengdu, 2017.

[50] Z. W. Chen, G. W. Gao, D. J. Yu, and S. Liu, "Resistivity measurement of irregularly-shaped graphite heater: a simulation and experiment study," *Chinese Journal of Vacuum Science and Technology.*, vol. 38, no. 9, pp. 810–816, 2018.

[51] C. S. Hu, J. H. Luo, P. Wang, L. R. Che, C. Z. Zhang, and N. Yin, "Characteristics research on resistivity of gold-bearing pyrite in the Linglong gold deposit," *Bulletin of Mineralogy, Petrology and Geochemistry.*, vol. 30, no. 2, pp. 156–159, 2011.

[52] Y. Bernabé, M. Li, and A. Maineult, "Permeability and pore connectivity: a new model based on network simulations," *Journal of Geophysical Research*, vol. 115, pp. 1–14, 2010.

[53] Y. Bernabé, M. Zamora, M. Li, and Y. B. Tang, "Pore connectivity, permeability, and electrical formation factor: a new model and comparison to experimental data," *Journal of Geophysical Research*, vol. 116, pp. 1–15, 2011.

[54] M. Li, Y. B. Tang, Y. Bernabe et al., "Pore connectivity, electrical conductivity, and partial water saturation: network simulations," *Journal of Geophysical Research: Solid Earth*, vol. 120, no. 6, pp. 4055–4068, 2015.

[55] H. Wu, P. C. Fu, X. J. Yang et al., "Accurate imaging of hydraulic fractures using templated electrical resistivity tomography," *Geothermics*, vol. 8, pp. 74–87, 2019.

[56] H. Lee, J. Lee, and T. Oh, "Permeability evaluation for artificial single rock fracture according to geometric aperture variation using electrical resistivity," *Journal of Rock Mechanics and Geotechnical Engineering*, vol. 13, no. 4, pp. 787–797, 2021.

[57] S. Lee, A. Khaiful, and N. Muhammad, "High-resolution electrical resistivity tomography and seismic refraction for groundwater exploration in fracture hard rocks: a case study in Kanthan, Perak, Malaysia," *Journal of Asian Earth Sciences*, vol. 218, pp. 1–17, 2021.

[58] Z. H. Zhang, *Fluid Mechanics (2nd Edition)*, Tsinghua University Press, Beijing, 2011.

[59] J. H. He, M. Li, K. M. Zhou et al., "Radial resistivity measurement method for cylindrical core samples," *Interpretation*, vol. 8, no. 4, pp. 1071–1080, 2020.

[60] W. L. Xiao, Y. B. Yang, M. Li et al., "Pore experimental study on the relationship between capillary pressure and resistivity index in tight sandstone rocks," *Petrophysics*, vol. 62, no. 4, pp. 434–446, 2021.

[61] L. Z. Cheng, Y. Wang, and C. Zhang, "Anisotropy of complex resistivity of the shale in eastern Guizhou province and its correlations to reservoir parameters of shale gas," *Chinese Journal of Geophysics*, vol. 64, no. 9, pp. 3344–3357, 2021.

[62] Q. S. Meng, X. Tong, X. L. Zheng, Z. Li, and Y. Q. Fan, "An experimental investigation of relationship of chloride concentration and mineralization with resistivity in saltwater intrusion zone of Dagu River," *Periodical of Ocean University of China*, vol. 45, no. 5, pp. 87–92, 2015.